A three-dimensional plastic-damage model for polymer composite materials

I.R. Cózar [a],[*], F. Otero [b],[c], P. Maimí [a], E.V. González [a], S. Miot [d], A. Turon [a], P.P. Camanho [e],[f]

[a] *AMADE, Polytechnic School, University of Girona, Campus Montilivi s/n, 17071 Girona, Spain*
[b] *CIMNE, Universitat Politècnica de Catalunya, 08034 Barcelona, Spain*
[c] *Department of Nautical Science and Engineering, Universitat Politècnica de Catalunya, Pla de Palau 18, 08003 Barcelona, Spain*
[d] *IRT Saint Exupéry, 31405 Toulouse, France*
[e] *DEMec, Faculdade de Engenharia, Universidade do Porto, 4200-465 Porto, Portugal*
[f] *INEGI, Instituto de Ciência e Inovação em Engenharia Mecânica e Industrial, 4200-465 Porto, Portugal*

ARTICLE INFO

ABSTRACT

A new 3D elastoplastic damage model is proposed to predict the plastic deformation and the progressive failure of unidirectional laminated composite materials at the meso-scale level. A non-associated flow rule is employed to properly define the volumetric plastic strains. The damage evolution laws are defined to account for the failure mechanisms on the longitudinal and transverse directions. Off-axis compressive and tensile tests with different ply orientations and high plastic dependency are used to demonstrate the ability of the model to capture the plastic response and the damage onset as well as the fracture planes. In addition, open-hole compressive and tensile tests with different dimensions are carried out to demonstrate the capability of the model to predict the failure strength. Good agreement is obtained between the numerical and experimental data.

1. Introduction

Advanced fibre-reinforced polymer (FRP) composite materials are increasingly used in complex structures in the mobility industry. In the particular case of the aerospace industry, airworthiness certification is required, which implies extensive experimental test campaigns to characterise the mechanical response of composite structures. To reduce the size of the test campaigns, efficient and reliable numerical tools are required. One solution is to link constitutive models with Finite Element (FE) simulations.

The nonlinearity due to plastic deformation of the FRP composite materials causes a stress redistribution affecting the onset of the failure mechanisms. Koerber et al. [1,2] studied the mechanical response of a FRP composite material at different strain rates (quasi-static and high strain rates). The authors carried out off-axis and transverse tests in compression and in tension. While the experimental data showed considerable plastic deformation for both strain rates and loading directions, compression leads to higher plastic deformation. Chen et al. [3] performed off-axis compressive and tensile tests with E-glass fibre-reinforced polymer composite material. The experimental data also showed significant plasticity. Moreover, the mechanical behaviour of FRP composite materials depend on hydrostatic pressure [4,5]. This dependency requires the use of elastoplastic material models with a non-associative flow rule to properly capture the plastic dilatancy or

contractility. In addition, out-of-plane stresses are insignificant when laminated composite materials are used in thin structures where in-plane stresses dominate the stress state away from free-edges. However, composite laminates are used in complex geometries where it critical to capture the effects of out-of-plane stresses [6]. Therefore, 3D material models are needed to capture the inelastic deformation and fracture behaviour in out-of-plane stress states (e.g. shear yielding and the fracture strengths affected by the hydrostatic pressure [4,5], three-dimensional stress states effect the failure of pressure vessels [7], 3-point bending tests to predict the out-of-plane tensile strength [8], bolted composite joints with clamping pressure, in impact tests, in curved structures, etc.), but also under the in-plane stress states (e.g. tests with in-plane boundary conditions where interface damage plays a relevant role). Plasticity models and continuum damage mechanics formulation are often used to predict the nonlinear mechanical response of FRP composite materials.

Chen et al. [9] developed an elastoplastic damage model to predict the mechanical response of a unidirectional FRP composite material assuming plane stress conditions. The plasticity model was based on the model presented by Sun and Chen [10]. An isotropic yield function and an associated flow rule were used. The damage model was based on the Hashin's failure criteria with three damage variables to capture: fibre failure, matrix cracking due to a pure transverse load, and longitudinal

---

shear stiffness degradation from fibre failure and matrix cracking. The damage evolution was described with exponential softening laws. The onset of damage was validated by comparing the numerical failure predictions with the failure strength from open-hole tensile tests. In general, good predictions were found, although the relative error was higher than 15% for 4 of the 17 cases studied. In addition, an in-plane shear test was simulated. The results showed a good prediction of the plastic strain but an under-prediction of the failure strength. Hoffarth et al. [11] proposed an elastoplastic damage model to predict the mechanical behaviour of a unidirectional FRP composite material under impact load. The yield function of the plasticity model was defined using the Tsai–Wu composite failure criterion [12]. A new non-associated flow rule was proposed to define the evolution of the plastic strains. The onset and propagation of the damage were based on the work of Matzenmiller et al. [13]. The authors compared the out-of-plane displacement vs. time curve obtained from an impact test with the numerical predictions. The predicted curve accurately captured the positive and negative peak displacement values of the first cycle and the displacement profile around the first peak. However, the peak displacements were overestimated for the subsequent cycles. Xie et al. [14] presented an elastoplastic damage model to describe the mechanical response of a carbon fibre reinforced carbon–silicon carbide (C/C-SiC) composite material in plane stress conditions. The authors proposed a new yield function as a function of the in-plane stresses and the material properties, and an associated flow rule was used. Three damage variables were used to degrade the in-plane elastic material properties. The evolution of each damage variable was defined using an exponential function. The material model was validated by comparing the plastic response to the one obtained from experimental data. Off-axis tensile and in-plane shear curves were predicted with a good agreement. The plastic deformations were correctly evaluated. In addition, the load–displacement, load-plastic strain and load–strain curves from a single open-hole tensile test were compared with the corresponding predictions. Again, the material model properly captured the plastic response. Holthusen et al. [15] developed a constitutive model for unidirectional fibre composite materials. The plasticity model was based on Von Mises yield criterion with an associated flow rule. Three damage variables were used: two associated to the fibre (tension and compression damage) and one for the matrix. The authors only showed the simulated response of the material under cyclic uniaxial tensile–compressive loading and the interaction between the fibre and matrix damage. Open-hole virtual tests were also performed with different conditions on the material model (activating/deactivating plasticity and damage). Chen et al. [3] proposed an elastoplastic damage model to describe the plastic hardening response and damage evolution. The modified Drucker–Prager yield criterion proposed by Cho et al. [16] was employed to account for the deviatoric and dilatational plastic deformation. In addition, the authors added a term in the yield function to prevent compressive stresses from generating shear yielding based on the work of Daniel [17]. An associated flow rule was used. The damage activation functions was based on the Puck failure criteria [18,19]. Exponential damage laws were used to model the degradation of the elastic material properties in the principal directions. The model was validated by simulating off-axis compressive and tensile tests. The comparison with the experimental test showed good agreement of the stress vs. strain curves and the failure strengths.

There is a need to develop an elastoplastic damage model using: a non-associated plastic flow rule to capture the plastic dilatancy or contractility, a 3D material model to account out-of-plane loading conditions, and an extensive comparison of the numerical predictions with experimental data. Therefore, the objective of this work is to develop a reliable constitutive model to predict the plastic deformation and the progressive failure of FRP composite materials at the meso-scale level. The main features of the material model are: (i) the use of an additive decomposition of the infinitesimal strain tensor to account for the plastic effects, (ii) the plasticity modelling with a new plastic yield
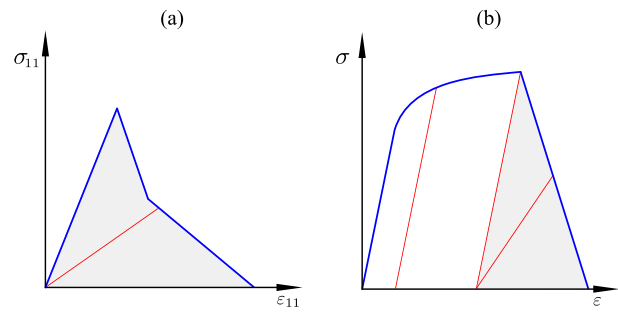

Fig. 1. Schematic representation of uniaxial stress vs. strain curve response at the material point level: (a) in the fibre direction, and (b) in the directions governed by the matrix.

function and a non-associated flow rule, (iii) a 3D damage model based on the model developed by Quintanas-Corominas et al. [20], (iv) the coupling between the plasticity and damage model, and (v) the material data cards can be measured from well-established experimental tests. The constitutive model is described in Section 2 and its implementation in Section 3. The capabilities of the model has been demonstrated by comparing the numerical results with experimental data from off-axis compressive and tensile tests and open-hole compressive and tensile tests. Section 4 presents a detailed comparison of the stress vs. strain curves, the failure strength and the fracture planes.

2. Constitutive model

The proposed material model is developed within the framework of the infinitesimal strain theory. The strain tensor is composed as

$$\varepsilon = \varepsilon^e + \varepsilon^p, \tag{1}$$

where ε^e is the elastic strain tensor (it includes cracking strains) and ε^p is plastic strain tensor.

It is assumed that in the fibre direction of the homogenised composite materials no plasticity occurs, and the model describes the elastic response until the onset of damage. Then, longitudinal fibre failure occurs in the absence of plasticity deformation, see Fig. 1a. However, in the directions governed by the matrix, the material model initially represents an elastic behaviour until the onset of plasticity is reached. It is assumed that when the matrix crack is initialised, plasticity cannot grow at the material point level, see Fig. 1b.

A new plasticity model has been developed and combined with a damage model (see Fig. 1b) based on the constitutive model presented by Quintanas-Corominas et al. [20]. Therefore, the complementary Gibbs free-energy density W proposed in [20] is used. It depends on four of the five invariants of the stress tensor (σ) at a rotation with respect to the longitudinal axis: the longitudinal stress σ_ℓ (i.e. fibre direction); the transverse hydrostatic pressure p_t; τ_ℓ and τ_t which are related with the longitudinal shear stress and the transverse shear stress, respectively. The function W is defined as:

$$W := \frac{\sigma_\ell^2}{2(1-d_\ell)E_{11}} - \frac{2v_{12}\sigma_\ell p_t}{E_{11}} + \frac{p_t^2}{2(1-d_t)E_t} + \frac{\tau_t^2}{2(1-d_{st})G_t}$$
$$+ \frac{\tau_\ell^2}{2(1-d_{s\ell})G_{12}} + \sigma\varepsilon^p, \tag{2}$$

where E_{11} is the longitudinal elastic modulus, v_{12} is the longitudinal Poisson's ratio and G_{12} is the longitudinal shear elastic modulus. E_t and G_t are the bulk and shear elastic stiffness in the transverse isotropic plane, respectively, which are defined as

$$E_t := \frac{E_{22}}{2(1-v_{23})} \tag{3}$$

and

$$G_t := \frac{E_{22}}{2(1 + \nu_{23})}, \tag{4}$$

where E_{22} is the transverse elastic modulus and ν_{23} is the transverse Poisson's ratio. The stress invariants are defined as:

$$\sigma_\ell = \boldsymbol{\sigma}_{11}, \tag{5}$$

$$p_t = \frac{\boldsymbol{\sigma}_{22} + \boldsymbol{\sigma}_{33}}{2}, \tag{6}$$

$$\tau_\ell = \sqrt{\boldsymbol{\sigma}_{12}^2 + \boldsymbol{\sigma}_{13}^2} \tag{7}$$

and

$$\tau_t = \frac{\sqrt{(\boldsymbol{\sigma}_{22} - \boldsymbol{\sigma}_{33})^2 + 4\boldsymbol{\sigma}_{23}^2}}{2}, \tag{8}$$

where $\boldsymbol{\sigma}_{ij}$ are the Cartesian components of the stress tensor $\boldsymbol{\sigma}$. The scalar variable $d_{M=\ell,t,s\ell,st}$ describes the damage state in the corresponding direction. The subscript ℓ refers to longitudinal (i.e. fibre), t refers to transverse (i.e. matrix) and s refers to shear. The material is undamaged for $d_M = 0$, it is damaged for $0 < d_M \leq 1$, and it is fully damaged for $d_M = 1$.

The strain tensor is obtained from the Clausius–Duhem inequality [21,22] as the derivative of W with respect to the mechanical stresses as

$$\varepsilon = \frac{\partial W}{\partial \boldsymbol{\sigma}} = \mathbb{H}\boldsymbol{\sigma} + \varepsilon^p, \tag{9}$$

where $\mathbb{H}$ is the compliance tensor and it can be expressed in Voigt Notation as

$$\mathbb{H} = \begin{bmatrix} \mathbb{H}_{11} & \mathbb{H}_{12} & \mathbb{H}_{12} & 0 & 0 & 0 \\ \mathbb{H}_{12} & \mathbb{H}_{22} & \mathbb{H}_{23} & 0 & 0 & 0 \\ \mathbb{H}_{12} & \mathbb{H}_{23} & \mathbb{H}_{22} & 0 & 0 & 0 \\ 0 & 0 & 0 & \mathbb{H}_{44} & 0 & 0 \\ 0 & 0 & 0 & 0 & \mathbb{H}_{55} & 0 \\ 0 & 0 & 0 & 0 & 0 & \mathbb{H}_{55} \end{bmatrix} \tag{10}$$

with:

$$\mathbb{H}_{11} = \frac{1}{(1 - d_\ell)E_{11}}$$

$$\mathbb{H}_{12} = -\frac{\nu_{12}}{E_{11}}$$

$$\mathbb{H}_{22} = \frac{1}{4(1 - d_t)E_t} + \frac{1}{4(1 - d_{st})G_t}$$

$$\mathbb{H}_{23} = \frac{1}{4(1 - d_t)E_t} - \frac{1}{4(1 - d_{st})G_t} \tag{11}$$

$$\mathbb{H}_{44} = \frac{1}{(1 - d_{st})G_t}$$

$$\mathbb{H}_{55} = \frac{1}{(1 - d_{s\ell})G_{12}}.$$

2.1. Modelling plasticity

A scalar function is proposed as the yield function, which depends on the stress invariants, and the equivalent plastic strain $\bar{\varepsilon}^p$ since the yield stresses are defined as a function of $\bar{\varepsilon}^p$. The yield function is developed from the transverse loading function proposed by Quintanas-Corominas et al. [20], because it is a convex function homogeneous of degree one. In addition, it is a single function to define a closed yield surface instead of using multiple equations as formulated in other models (e.g. using one for compression and one for tension depending

on the hydrostatic pressure in the matrix [2]). Therefore, the yield function reads

$$\phi^p(\boldsymbol{\sigma}, \bar{\varepsilon}^p) := \sqrt{\left(\frac{Y_{CP} + Y_{TP}}{Y_{CP}Y_{TP}}\right)^2 \frac{\tau_t^2 + \mu_{tp}p_t^2}{1 + \mu_{tp}} + \left(\frac{\mu_{s\ell p}}{S_{LP}}\tau_\ell\right)^2}$$
$$+ \frac{Y_{CP} - Y_{TP}}{Y_{CP}Y_{TP}}p_t + \frac{(1 - \mu_{s\ell p})}{S_{LP}}\tau_\ell - 1 \leq 0, \tag{12}$$

where Y_{TP} and Y_{CP} are the transverse uniaxial tensile and compressive yield stresses, respectively, and S_{LP} is the longitudinal shear yield stress. $\mu_{s\ell p}$ and μ_{tp} are the plastic envelope shape coefficients, whose calibration is presented in Section 2.3. These parameters allow different shapes of the yield surface to be defined, depending on the mechanical response of the material to be analysed (see Fig. 2a and b replacing the damage parameters by the corresponding plastic parameters, e.g. Y_T by Y_{TP}).

The yield function of Eq. (12) allows a control of the activation of the yielding for uniaxial loads in the transverse direction in tension and in compression, as well as for longitudinal shear loading states by means of the corresponding yield stresses. Furthermore, the plasticity can be activated under other transverse loading conditions controlled by μ_{tp} and $\mu_{s\ell p}$. For example, shear yielding in the longitudinal or transverse direction is affected by the transverse hydrostatic pressure as observed in [4,5]: the higher the transverse compressive hydrostatic is, the higher the shear yielding is.

The evolution of the equivalent plastic strain rate is defined as

$$\dot{\bar{\varepsilon}}^p := \sqrt{\frac{1}{2}} \left\| \dot{\varepsilon}^p \right\|, \tag{13}$$

where $\dot{\varepsilon}^p$ is the plastic strain rate. The evolution of the plastic strains is defined using the gradient of the potential function φ^p, see Eq. (21). Hence, a non-associated flow rule is applied in the present model. That allows the volumetric plastic strains and the plastic Poisson's ratios to be imposed. Therefore, the plastic strain rate is defined as

$$\dot{\varepsilon}^p := \lambda \partial_{\boldsymbol{\sigma}} \varphi^p, \tag{14}$$

where λ is the plastic multiplier parameter [25]. The loading/unloading conditions are applied using the following Kuhn–Tucker conditions to calculate λ:

$$\phi^p \leq 0, \quad \lambda \geq 0. \tag{15}$$

Therefore, under plastic loading $\phi^p = 0$ and $\lambda > 0$, and for unloading $\phi^p < 0$ and $\lambda = 0$. Hence:

$$\phi^p \lambda = 0. \tag{16}$$

These condition can be summarised in the consistency condition as:

$$\dot{\phi}^p \lambda = 0. \tag{17}$$

The plastic multiplier parameter λ can be calculated in case of plastic loading ($\phi^p = 0$ and $\lambda > 0$) imposing the following condition

$$\dot{\phi}^p = \partial_{\boldsymbol{\sigma}} \phi^p \dot{\boldsymbol{\sigma}} + \partial_{\bar{\varepsilon}^p} \phi^p \dot{\bar{\varepsilon}}^p = 0. \tag{18}$$

Inserting Eqs. (13) and (14) in the previous conditions

$$\dot{\phi}^p = \partial_{\boldsymbol{\sigma}} \phi^p \mathbb{C}_e (\dot{\varepsilon} - \lambda \partial_{\boldsymbol{\sigma}} \varphi^p) + \partial_{\bar{\varepsilon}^p} \phi^p \lambda \sqrt{\frac{1}{2}} \left\| \partial_{\boldsymbol{\sigma}} \varphi^p \right\| = 0, \tag{19}$$

the plastic multiplier parameter yields

$$\lambda = \frac{\partial_{\boldsymbol{\sigma}} \phi^p \mathbb{C}_e \dot{\varepsilon}}{\partial_{\boldsymbol{\sigma}} \phi^p \mathbb{C}_e \partial_{\boldsymbol{\sigma}} \varphi^p - \sqrt{\frac{1}{2}} \partial_{\bar{\varepsilon}^p} \phi^p \left\| \partial_{\boldsymbol{\sigma}} \varphi^p \right\|}. \tag{20}$$

Finally, the plastic potential function is defined as

$$\varphi^p(\boldsymbol{\sigma}) := \sqrt{\left(\frac{\hat{Y}_{CP} + \hat{Y}_{TP}}{\hat{Y}_{TP}\hat{Y}_{CP}}\right)^2 \frac{\tau_t^2 + \hat{\mu}_{tp}p_t^2}{1 + \hat{\mu}_{tp}} + \left(\frac{\hat{\mu}_{s\ell p}}{\hat{S}_{LP}}\tau_\ell\right)^2}$$
$$+ \frac{\hat{Y}_{CP} - \hat{Y}_{TP}}{\hat{Y}_{TP}\hat{Y}_{CP}}p_t + \frac{(1 - \hat{\mu}_{s\ell p})}{\hat{S}_{LP}}\tau_\ell - 1. \tag{21}$$
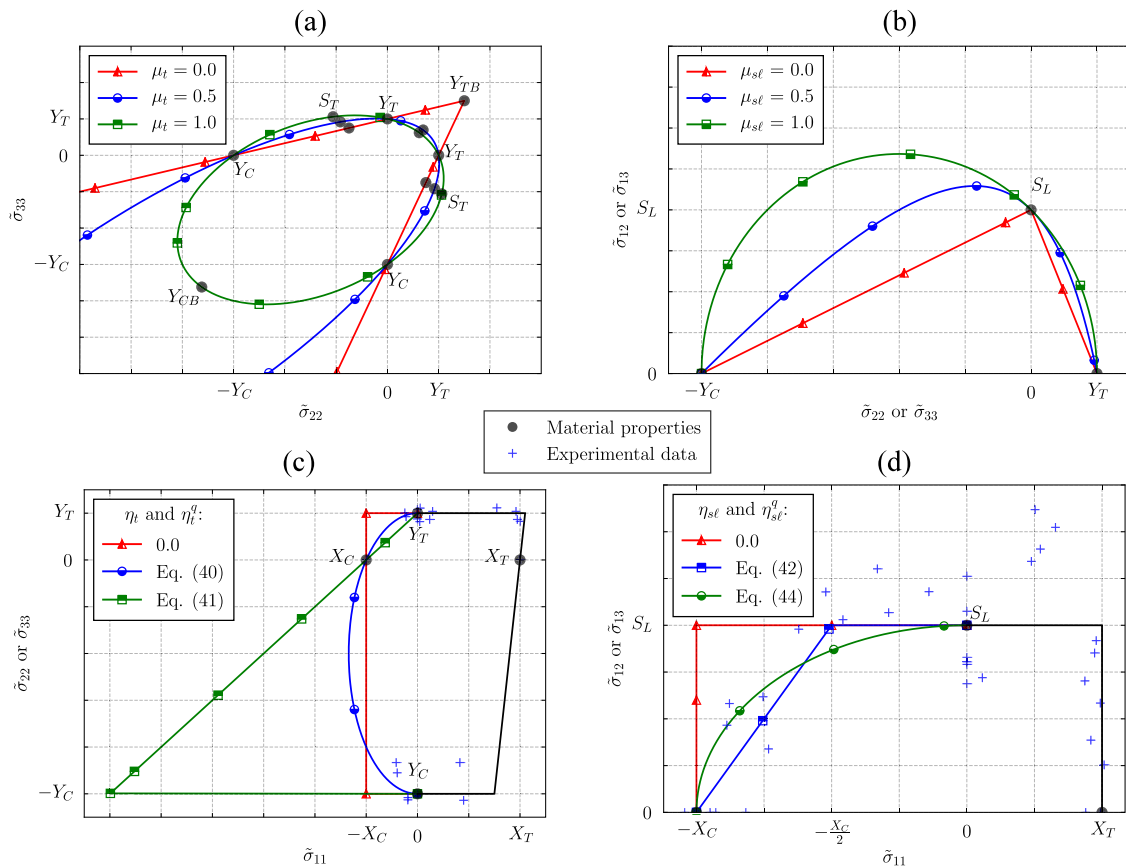
Fig. 2. Schematic representation of the failure envelope for the stress space: (a) $\tilde{\sigma}_{22} - \tilde{\sigma}_{33}$, (b) $\tilde{\sigma}_{22} - \tilde{\sigma}_{12}$, (c) $\tilde{\sigma}_{11} - \tilde{\sigma}_{22}$, and (d) $\tilde{\sigma}_{11} - \tilde{\sigma}_{12}$. Note that, (b) and (d) are symmetric with respect to their *X*-axis. The experimental data in (c) from [23] is used to propose Eq. (40), and (d) from [24] for Eq. (42), see Section 2.3.

Eq. (21) has the same form as the yield function but each yield stress and plastic envelope shape coefficients are replaced by the corresponding plastic potential parameters. The plastic potential stresses $\hat{Y}_{CP}$, $\hat{Y}_{TP}$ and $\hat{S}_{LP}$ and the plastic potential envelope shape coefficients $\hat{\mu}_{tp}$ and $\hat{\mu}_{s\ell p}$ are defined as constant parameters. They do not have a physical meaning, they are used to control the plastic dilatancy or contractility in the plastic zone (these parameters define the direction of the plastic flow). For this reason, only the ratios between them are relevant and not their absolute values. Note that, if the plastic potential stresses are set equal to the yield stresses, the plasticity would be modelled using an associated flow rule.

The plastic dilatancy or contractility is defined using three plastic Poisson's ratios: v_{23T}^p and v_{23C}^p are the transverse tensile and compressive Poisson's ratios, respectively, and $v_{122}^p := -\dfrac{\varepsilon_{22}^p}{\varepsilon_{12}^p}$. They can be measured by three tests: pure transverse tensile test (v_{23T}^p), pure transverse compressive test (v_{23C}^p) and pure longitudinal shear test (v_{122}^p). It should be noted that, these tests are also used to adjust the yield function. Hence, the total number of tests required to calibrate the plasticity input parameters does not increase. The plastic potential ratios are defined as

$$
\begin{aligned}
\frac{\hat{Y}_{CP}}{\hat{Y}_{TP}} &= \frac{v_{23C}^p + 1}{v_{23T}^p + 1} \\[2mm]
\frac{\hat{S}_{LP}}{\hat{Y}_{TP}} &= \frac{2 v_{122}^p (v_{23C}^p + 1)}{v_{23T}^p - v_{23C}^p} \\[2mm]
\hat{\mu}_{tp} &= \frac{1 - v_{23C}^p v_{23T}^p}{(v_{23C}^p + 1)(v_{23T}^p + 1)} \\[2mm]
\hat{\mu}_{s\ell p} &\in \mathbf{R}.
\end{aligned}
\tag{22}
$$

However, if there is no volumetric plastic strains ($v_{23T}^p = v_{23C}^p = 1$ and $v_{122}^p = 0$), the plastic potential relationships are simplified to

$$
\begin{aligned}
\frac{\hat{Y}_{CP}}{\hat{Y}_{TP}} &= 1 \\[2mm]
\hat{S}_{LP} &\in \mathbf{R} \\[2mm]
\hat{\mu}_{tp} &= 0 \\[2mm]
\hat{\mu}_{s\ell p} &\in \mathbf{R}.
\end{aligned}
\tag{23}
$$

2.2. Modelling damage evolution

The evolution of the damage is based on the model developed by Quintanas-Corominas et al. [20]. The model is based on the crack band model of Bažant and Oh [26] to ensure the proper energy dissipation when the crack propagates. The degradation of the elastic properties is modelled by four softening laws. The evolution of the damage variables is defined as a function of the corresponding elastic domain threshold $r_{N=\ell T,\ell C,t}$. $d_\ell(r_{\ell T}, r_{\ell C})$ is associated to the first stress invariant σ_ℓ and model the longitudinal failure in tension ($\sigma_\ell > 0$) and in compression ($\sigma_\ell < 0$); $d_t(r_t)$ is related to the mode-I matrix cracking associated to the second stress invariant p_t; $d_{st}(r_t)$ describes the mode-II matrix cracking associated to the third stress invariant τ_t; and $d_{s\ell}(r_t, r_{\ell T})$ is linked to the longitudinal tensile and matrix damage mechanisms associated to the stress invariant τ_ℓ.

Three loading functions are employed to consider the previously explained damage mechanisms: $\phi_{\ell T}$ for the fibre breakage, $\phi_{\ell C}$ for the fibre kinking, and ϕ_t for the matrix cracking. They read

$$
\phi_{\ell T} := \frac{\tilde{\sigma}_\ell - 2 v_{12} \tilde{p}_t}{X_T},
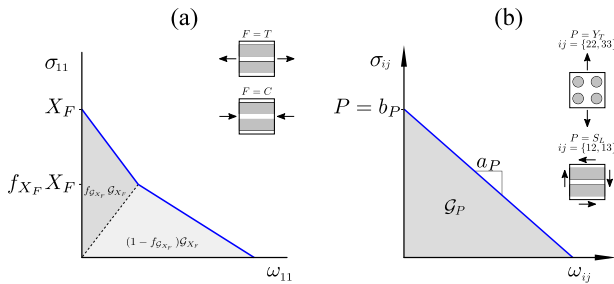\tag{24}
$$

Fig. 3. Stress vs. opening crack curves of the cohesive law in the directions: (a) longitudinal and (b) transverse.

$$\phi_{\ell C} := \frac{1}{X_C} \left(\sqrt{\tilde{\sigma}_\ell^2 + \eta_t^q \tilde{p}_t^2 + \eta_{s\ell}^q \tilde{\tau}_\ell^2} + \eta_t \tilde{p}_t + \eta_{s\ell} \tilde{\tau}_\ell \right) \tag{25}$$

and

$$\phi_t := \sqrt{\left(\frac{Y_C + Y_T}{Y_T Y_C} \right)^2 \frac{\tilde{\tau}_t^2 + \mu_t \tilde{p}_t^2}{1 + \mu_t} + \left(\frac{\mu_{s\ell}}{S_L} \tilde{\tau}_\ell \right)^2} \tag{26}$$
$$+ \frac{Y_C - Y_T}{Y_T Y_C} \tilde{p}_t + \frac{(1 - \mu_{s\ell})}{S_L} \tilde{\tau}_\ell,$$

where X_T and X_C are the longitudinal tensile and compressive strengths, respectively; Y_T and Y_C are the transverse tensile and compressive strengths, respectively; and S_L is the longitudinal shear strength. The effective stress invariants $\tilde{\sigma}_\ell$, $\tilde{p}_t$, $\tilde{\tau}_\ell$ and $\tilde{\tau}_t$ are obtained from the effective stress tensor $\tilde{\sigma}$ using the elasticity tensor in the absence of damage $\left(\mathbb{C}_{e0} = \mathbb{H}^{-1}(d_M = 0) \right)$. The damage envelope shape coefficients: η_t and η_t^q are related to the transverse hydrostatic pressure and the longitudinal compressive strength; $\eta_{s\ell}$ and $\eta_{s\ell}^q$ are associated to the longitudinal compressive and longitudinal shear strengths; μ_t is governed by the transverse shear and transverse biaxial strengths; and $\mu_{s\ell}$ is linked to the transverse and longitudinal shear strengths, see Fig. 2. Section 2.3 describes how to adjust them.

The corresponding elastic domain threshold is calculated by integrating its corresponding loading function with respect to time applying the Kuhn–Tucker relations [22]. It can be explicitly integrated as

$$r_N = \max \left(1, \max_{s \in [0,t]} \left(\phi_N^s \right) \right), \tag{27}$$

since the loading functions are defined only as a function of the strain tensor.

The expressions of the evolution of the damage variables as a function of the corresponding elastic domain threshold presented by Quintanas-Corominas et al. [20] are used, except for d_{st}. The longitudinal damage variable d_ℓ is defined as

$$d_\ell := d_{\ell T} \frac{\langle \sigma_\ell \rangle}{|\sigma_\ell|} + d_{\ell C} \frac{\langle -\sigma_\ell \rangle}{|\sigma_\ell|}, \tag{28}$$

where $\langle x \rangle = (x + |x|)/2$ is the McCauley operator. Therefore, if the first stress invariant is positive ($\sigma_\ell > 0$), then $d_\ell = d_{\ell T}$, otherwise $d_\ell = d_{\ell C}$. This allows a different longitudinal damage evolution in tension than in compression. The softening law in the longitudinal tensile direction $d_{\ell T}$ is defined using a bilinear law, in the same way as in [27,28]. The first segment is defined with a large drop stress due to the fibre breakage followed by a large tail related to the fibre pull-out, see Fig. 3a.

The damage variable in the longitudinal compressive direction $d_{\ell C}$ is defined using a bilinear cohesive law, in the same way as [27,28]. The first segment defines the kink-band onset using a large drop followed by an horizontal asymptote related to kink-band broadening and frictional contact.

It is assumed that the degradation of the matrix stiffness due to mode-I matrix cracking is the same that the one generated by mode-II

matrix cracking when the crack opens ($p_t > 0 \rightarrow d_t = d_{st}$). However, there is no degradation of the matrix stiffness in mode-I when the crack closes ($p_t < 0 \rightarrow d_t = 0$). Therefore, the transverse damage variable d_t is defined equal to the transverse shear damage variable d_{st} when the second invariant p_t is positive, and equal to zero when the second invariant is negative,

$$d_t := d_{st} \frac{\langle p_t \rangle}{|p_t|}. \tag{29}$$

The damage variable d_{st} is defined assuming a linear cohesive law from a pure transverse tensile test. The cohesive law is defined with a slope of a_{Y_T} and an intercept of b_{Y_T}, see Fig. 3b. It is established as a function of the elastic domain threshold r_t in Eq. (26) as

$$d_{st} = -\sqrt{-\frac{\kappa_{2_{st}}}{\kappa_{0_{st}}} + \frac{\kappa_{1_{st}}^2}{4\kappa_{0_{st}}^2}} - \frac{\kappa_{1_{st}}}{2\kappa_{0_{st}}} \tag{30}$$

with:

$$\kappa_{0_{st}} = \mathbb{H}_{0_{12}}^2 \kappa_{5_{st}} \left(\mathbb{H}_{0_{22}} - \mathbb{H}_{0_{23}} \right) + 4 S_T^2 \kappa_{4_{st}}^2$$
$$\kappa_{1_{st}} = \kappa_{5_{st}} \kappa_{6_{st}} - 4 S_T^2 \kappa_{4_{st}} \kappa_{3_{st}}$$
$$\kappa_{2_{st}} = \left(S_T \kappa_{3_{st}} \right)^2 - \left(\mu_t + 1 \right) \left(Y_C Y_T b_{Y_T} \kappa_{6_{st}} \right)^2$$
$$\kappa_{3_{st}} = 2 Y_C Y_T \kappa_{6_{st}} r_t + b_{Y_T} \kappa_{7_{st}} \left(Y_C - Y_T \right)$$
$$\kappa_{4_{st}} = \mathbb{H}_{0_{12}}^2 b_{Y_T} \left(\mathbb{H}_{0_{22}} - \mathbb{H}_{0_{23}} \right) \left(Y_C - Y_T \right) + Y_C Y_T \kappa_{6_{st}} r_t \left(\mathbb{H}_{0_{22}} a_{Y_T} l_t^* + 1 \right)$$
$$\kappa_{5_{st}} = \mu_t \left(\mathbb{H}_{0_{23}} - \mathbb{H}_{0_{22}} \right) \left(2 \mathbb{H}_{0_{12}} Y_C Y_T b_{Y_T} \right)^2$$
$$\kappa_{6_{st}} = \mathbb{H}_{0_{11}} (\mathbb{H}_{0_{22}}^2 - \mathbb{H}_{0_{23}}^2) + 2 \mathbb{H}_{0_{12}}^2 (\mathbb{H}_{0_{23}} - \mathbb{H}_{0_{22}})$$
$$\kappa_{7_{st}} = 2 \mathbb{H}_{0_{12}}^2 \left(\mathbb{H}_{0_{22}} - \mathbb{H}_{0_{23}} \right) + (\mathbb{H}_{0_{22}} + \mathbb{H}_{0_{23}}) \left(\mathbb{H}_{0_{11}} \mathbb{H}_{0_{23}} - \mathbb{H}_{0_{11}} \mathbb{H}_{0_{22}} \right), \tag{31}$$

where l_t^* is the transverse characteristic element length. The transverse shear strength S_T can be obtained from Eq. (37) for a given μ_t. The intercept of the cohesive law b_{Y_T} is equal to Y_T and its corresponding slope reads

$$a_{Y_T} = -\frac{Y_T^2}{2 \mathcal{G}_{Y_T}}, \tag{32}$$

where $\mathcal{G}_{Y_T}$ is the mode-I intralaminar fracture toughness in the transverse tensile direction.

The longitudinal shear damage variable is defined as

$$d_{s\ell} := 1 - (1 - d_{s\ell*})(1 - d_{\ell T}), \tag{33}$$

where $d_{s\ell*}$ is the damage variable presented by Quintanas-Corominas et al. [20] and it is related to the longitudinal shear stresses. $d_{s\ell}$ allows the introduction of the stiffness degradation in the longitudinal shear direction due to longitudinal shear stresses σ_{12} and σ_{13}, but also due to longitudinal tensile stress σ_{11}.

2.3. Calibration of failure envelope

The calibration of the envelope shape coefficients of the plasticity and damage model is described in this section for FRP composite materials. First, the identification of the damage envelope shape coefficients is presented. Then, the same assumptions and approach can be used to estimate the plastic envelope shape coefficients replacing the strengths by the corresponding yield stresses.

The envelope shape coefficient μ_t controls the failure in the transverse shear direction S_T, but also in the biaxial compressive Y_{CB} and tensile Y_{TB} directions, see Fig. 2a. It can be calculated using the following expressions:

$$\mu_t(S_T) = \left(\frac{S_T(Y_C + Y_T)}{Y_C Y_T} \right)^2 - 1, \tag{34}$$

$$\mu_t(Y_{CB}) = \frac{\left(Y_C Y_T - Y_{CB}(Y_T - Y_C)\right)^2}{Y_{CB}^2(Y_C + Y_T)^2 - \left(Y_C Y_T - Y_{CB}(Y_T - Y_C)\right)^2} \tag{35}$$

or

$$\mu_t(Y_{TB}) = \frac{\left(Y_C Y_T - Y_{TB}(Y_C - Y_T)\right)^2}{Y_{TB}^2(Y_C + Y_T)^2 - \left(Y_C Y_T - Y_{TB}(Y_C - Y_T)\right)^2}, \tag{36}$$

where the expressions are obtained when $\phi_t = 0$ and applying a pure transverse shear stress state or the corresponding pure biaxial loading state, respectively. Significant difficulties occur when testing composite materials under transverse shear or biaxial loading [6]. Fenner and Daniel [29] proposed a methodology for transverse shear loading using a sandwich-beam under three-point bending test. Otherwise, S_T can be estimated from [30] as

$$S_T = \frac{Y_C}{2 \tan(\alpha_0)}, \tag{37}$$

assuming that the damage (or plasticity) occurs in the plane of maximum longitudinal shear stresses, where the value experimentally obtained of the angle of this plane α_0 is equal to $53°$, see [31].

The failure envelope for the $\sigma_{22} - \sigma_{12}$ stress space is defined using $\mu_{s\ell}$, see Fig. 2b. It can be calibrated by imposing that the slope at $\sigma_{22} = 0$ must be equal to the longitudinal matrix friction coefficient η_ℓ, as the Coulomb fracture line in the Mohr–Coulomb criterion. Therefore, it reads

$$\mu_{s\ell} = \frac{2\eta_\ell Y_C Y_T + S_L(Y_C - Y_T)}{4\eta_\ell Y_C Y_T}, \tag{38}$$

η_ℓ can be approximated from [31] as

$$\eta_\ell \approx -\frac{S_L \cos(2\alpha_0)}{Y_C \cos(\alpha_0)}. \tag{39}$$

Alternatively, $\mu_{s\ell}$ can be estimated from off-axis tests fitting the failure envelope (or yield surface) shape with the experimental data. Moreover, from the yield surfaces reported by Daniel [17] and failure envelopes from [17,30,32], $\mu_{s\ell}$ and $\mu_{s\ell p}$ must be defined close to one.

The envelope shape coefficients η_t and η_t^q are the coefficients of the linear and quadratic terms, respectively, related to the hydrostatic transverse pressure in $\phi_{\ell C}$. Therefore, they define the failure envelope for the $\tilde{\sigma}_{11} - \tilde{\sigma}_{22}$ stress space, see Fig. 2c. The experiments carried out by Soden et al. [24] suggest that these two parameters can be estimated for carbon FRP composite materials as

$$\eta_t = \frac{X_C(Y_C - Y_T)}{Y_C Y_T}$$
$$\eta_t^q = \left(\frac{X_C(Y_C + Y_T)}{Y_C Y_T}\right)^2. \tag{40}$$

Moreover, others envelopes can be defined, such as the slope equals to Y_T/X_C, where

$$\eta_t = \frac{2X_C}{Y_T}$$
$$\eta_t^q = 0. \tag{41}$$

The linear and quadratic terms related to the longitudinal shear stresses in $\phi_{\ell C}$ are $\eta_{s\ell}$ and $\eta_{s\ell}^q$, respectively. They define the failure envelope for the $\tilde{\sigma}_{11} - \tilde{\sigma}_{12}$ stress space, see Fig. 2d. They can be tuned for carbon FRP composites from the experimental data reported by Soden et al. [24] as

$$\eta_{s\ell} = \frac{X_C}{2S_L}$$
$$\eta_{s\ell}^q = 0, \tag{42}$$

hence, the slope is defined as $2S_L/X_C$. Furthermore, others envelopes can be defined: with the slope equals to S_L/X_C, where

$$\eta_{s\ell} = \frac{X_C}{S_L}$$
$$\eta_{s\ell}^q = 0; \tag{43}$$

or with perfect parabolic curve, where

$$\eta_{s\ell} = 0$$
$$\eta_{s\ell}^q = \left(\frac{X_C}{S_L}\right)^2. \tag{44}$$

Alternatively, the failure envelopes (or yield surfaces) can be estimated from the simulation of a representative cell (modelling polymer and fibres) under multiple multi-axial loading conditions combined with a data-driven approach [33,34]. After that, the envelope shape coefficients can be adjusted.

3. Implementation

The constitutive model presented in Section 2 is solved at the Gauss-point level using an explicit FE solver. The evolution of the plasticity internal variables (ε^p and $\bar{\varepsilon}^p$) is discretised in time using the backward Euler integration scheme and the operator split method: (i) an initial elastic predictor step, and (ii) a posterior plastic corrector step. However, the evolution of the internal damage variables (r_N) is carried out by integrating r_N into time using Eq. (27), therefore, they can be explicitly solved.

The algorithm of the material model time discretisation $t_{(n+1)}$ is presented in this section. The known data with respect to the previous increment of the time $t_{(n)}$ are the current total strain tensor at the end of the increment $\varepsilon_{(n+1)}$ and the internal variables at the beginning of the increment $\varepsilon_{(n)}^p$, $\bar{\varepsilon}_{(n)}^p$ and $r_{N_{(n)}}$.

Firstly, the damage model is evaluated to determine if the damage variables associated with the matrix cracking (d_t, $d_{s\ell}$ and d_{st}) are activated in the current time interval. If they are greater than zero, plasticity does not develop. However, if the matrix is undamaged ($d_t = d_{s\ell} = d_{st} = 0$), plasticity can evolve, see Fig. 1b. It is possible that the initiation of the matrix damage and an increase of the plastic strain tensor occur at the same time interval. In this case, the model assumes that the strain increment is only due to damage instead of damage and plasticity. This assumption produces a negligible error in the results, because very small time increments are used in explicit simulations.

Secondly, if the matrix is undamaged, the model calculates the increment of the plastic strains. For that, the elastic trial stress tensor is obtained assuming that there is no increase in the plastic strain tensor in the current time step $\left(\sigma_{(n+1)}^{tr} = \sigma_{(n+1)}(\Delta\varepsilon_{(n+1)}^p = 0)\right)$. Then, the yield function is evaluated with $\sigma_{(n+1)}^{tr}$ and $\bar{\varepsilon}_{(n)}^p$. If the yield function is less than zero (in this case, the bound is defined using a tolerance tol), there are no increment of plastic strains in the current time interval. However, if the yield function is greater than tol, the plastic strains increase in the current time interval. Therefore, the equivalent plastic strain that meets the condition in Eq. (12) must be found.

Applying the backward Euler algorithm at $t_{(n+1)}$ to be updated with $\gamma_{(n+1)} = \lambda_{(n+1)}(t_{(n+1)} - t_{(n)})$, where $\gamma_{(n+1)}$ is the consistency parameter. Therefore, the evolution of the plasticity equations read:

$$\varepsilon_{(n+1)}^p = \varepsilon_{(n)}^p + \gamma_{(n+1)} \partial_{\sigma_{(n+1)}} \varphi^p$$
$$\sigma_{(n+1)} = \sigma_{(n+1)}^{tr} - \gamma_{(n+1)} \mathbb{C}_e \partial_{\sigma_{(n+1)}} \varphi^p \tag{45}$$
$$\bar{\varepsilon}_{(n+1)}^p = \bar{\varepsilon}_{(n)}^p + \gamma_{(n+1)} \sqrt{\frac{1}{2}} \left\|\partial_{\sigma_{(n+1)}} \varphi^p\right\|.$$

The yield function condition from Eq. (12) gives an algebraic constraint that has to be fulfilled at the end of the current time step $(\phi_{(n+1)}^p(\sigma_{(n+1)}, \bar{\varepsilon}_{(n+1)}^p) = 0)$. It is solved with Newton–Raphson method for $\gamma_{(n+1)}$. The residual equation is developed in a Taylor-series and linearised as

$$\text{Lin}[R_{(n+1)}] = \phi_{(n+1)}^p + \frac{d\phi_{(n+1)}^p}{d\gamma_{(n+1)}} \Delta\gamma_{(n+1)} = 0. \tag{46}$$

Therefore, the linearisation of the residual is solved for the increment of the consistency parameter

$$\Delta\gamma_{(n+1)} = -\frac{\phi^p_{(n+1)}}{\frac{d\phi^p_{(n+1)}}{d\gamma_{(n+1)}}}. \tag{47}$$

Finally, the evolution of the plasticity internal variables is evaluated with the general convex cutting-plane algorithm presented by Simo and Hughes [25]. Algorithm 1 in Appendix summarises the workflow to implement the constitutive model using an explicit solver in a nonlinear FE framework.

4. Numerical predictions

Four cases are used to demonstrate the capabilities of the material model to predict not only the plastic deformation of composite materials, but also the onset and propagation of damage. Off-axis compressive and tensile tests with different ply orientations and high plastic dependency are used to demonstrate the ability of the model to capture the plastic response in Section 4.1. In addition, they are selected to demonstrate the capabilities of the model to predict the damage onset as well as the fracture planes when the failure mechanisms are matrix dominated. Open-hole tests under compressive and tensile loadings are used to present the potential of the model to predict the failure strength when the failure mechanisms are fibre dominated [35], see Section 4.2.

The experimental data are compared to the results of the corresponding FE models using the Abaqus/Explicit solver [36]. 3D eight-node C3D8R solid elements with reduced integration are used. The in-plane mesh element size is defined less or equal to 0.24 mm around the areas where damage is expected to occur to prevent snap-back of the constitutive softening laws for each failure mode [27]. Three elements through the thickness of each ply are used. In addition, elastic elements are defined in the regions where the damage is not expected to occur to reduce the computational time in the open-hole specimens, see Fig. 4b. Vertical displacement is applied on the top face at low velocity to avoid dynamic effects during the simulation.

In both loading cases, the laminates are manufactured using a carbon FRP composite material, IM7/8552 unidirectional prepreg system with a nominal thickness of 0.131 mm [35]. Table 1 summarises the model input parameters. The plastic envelope shape coefficients are fitted from the yield surface developed by Vogler et al. [37]. In addition, the plastic yield vs. equivalent plastic strain relationships are obtained from [37].

The transverse Poisson's ratio ν_{23} is assumed considering the value from [38], where the same polymer with different carbon fibre was used. The effect of ν_{23} on the numerical results is analysed. Different virtual tests are carried out with $\nu_{23} = \{0.3, 0.35, 0.40, 0.45\}$: off-axis in compression with a fibre orientation of 30° and another at 75° (see below section), and open-hole in compression with a hole diameter equal to 2 mm and in tensile with a diameter of 8 mm (see Section 4.2). No significant differences are found neither in the failure strength (the higher coefficient of variation from the numerical results is less than 0.4%) nor in the strains at the failure strength (the higher coefficient of variation is less than 2.5%) and in the stress–strain curves.

4.1. Off-axis tests

The off-axis compressive tests carried out by Koerber et al. [1] with the fibre angle orientations $\theta = 15°, 30°, 45°, 60°, 75°$ and 90° are simulated. In the numerical model, only the vertical displacements are fixed at the ends of the specimens. Additional boundary conditions are defined to avoid rigid body motions, see Fig. 4a. The in-plane dimensions of the specimens are 10 mm × 20 mm with 32 plies.

The stress vs. axial strain curves from the numerical simulations are compared with the experimental data in Fig. 5. The predicted failure strength of the specimens is in very good agreement with the test data at $\theta = 15°, 30°, 75°$ and 90°. However, failure is underestimated at $\theta = 45°$ and 60°. An explanation is that the experimental data
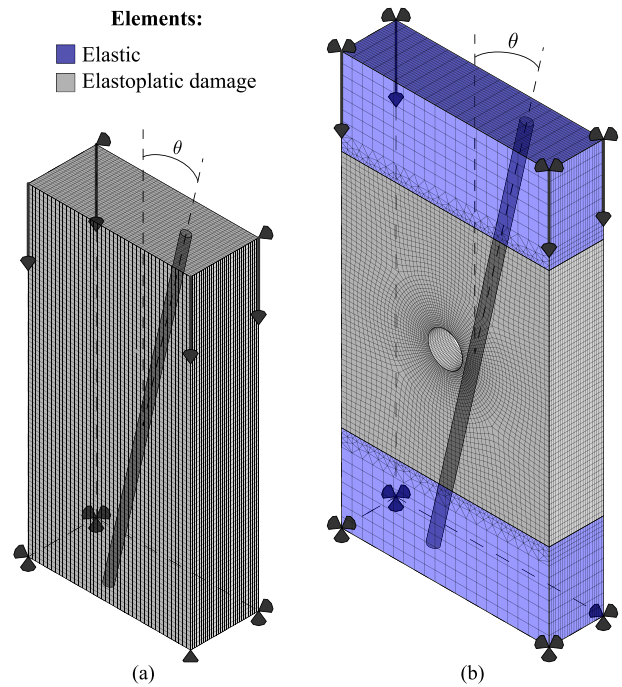
Elements:

Fig. 4. Schematic representation of the applied boundary conditions and the meshes used in the: (a) off-axis simulations, and (b) open-hole simulations. θ is the fibre angle orientation.

Table 1
Model input parameters for an IM7/8552 unidirectional prepreg system.

	Symbol	Value	Unit	Source
Elastic	E_{11}	171 420.00	MPa	[35]
	E_{22}	9 080.00	MPa	[35]
	G_{12}	5 290.00	MPa	[35]
	ν_{12}	0.32	–	[35]
	ν_{23}	0.45	–	Assumed
Plastic	$Y_{CP}(\bar{\varepsilon}^p)$	Curve		[37]
	$Y_{TP}(\bar{\varepsilon}^p)$	Curve		[37]
	$S_{LP}(\bar{\varepsilon}^p)$	Curve		[37]
	μ_{tp}	0.47	–	Adjusted in Section 4
	$\mu_{s\ell p}$	1.00	–	Adjusted in Section 4
	ν^p_{23T}	1.00	–	[37]
	ν^p_{23C}	1.00	–	[37]
	ν^p_{122}	0.00	–	[37]
Damage	X_C	1 017.50	MPa	[39]
	$f_{X_C} X_C$	203.50	MPa	[20]
	$\mathcal{G}_{X_C}$	106.30	N/mm	[35]
	$f_{\mathcal{G}_{X_C}} \mathcal{G}_{X_C}$	26.58	N/mm	[20]
	X_T	2 323.50	MPa	[39]
	$f_{X_T} X_T$	464.70	MPa	[20]
	$\mathcal{G}_{X_T}$	97.80	N/mm	[40]
	$f_{\mathcal{G}_{X_T}} \mathcal{G}_{X_T}$	48.90	N/mm	[20]
	Y_C	253.70	MPa	[20]
	Y_T	62.30	MPa	[35]
	$\mathcal{G}_{Y_T}$	0.28	N/mm	[35]
	S_L	92.30	MPa	[35]
	$\mathcal{G}_{S_L}$	0.80	N/mm	[35]
	μ_t	0.90	–	[20]
	$\mu_{s\ell}$	1.00	–	[20]
	$\eta_{s\ell}$	9.50	–	[20]
	$\eta^q_{s\ell}$	0.00	–	[20]
	η_t	12.00	–	[20]
	η^q_t	350.00	–	[20]

are out of the damage envelope, see Fig. 6. To obtain more accurate predictions, ϕ_t could be modified to fit the experimental data. The value defined here for $\mu_{s\ell}$ is in its upper bound ($\mu_{s\ell}$ =1). Moreover,
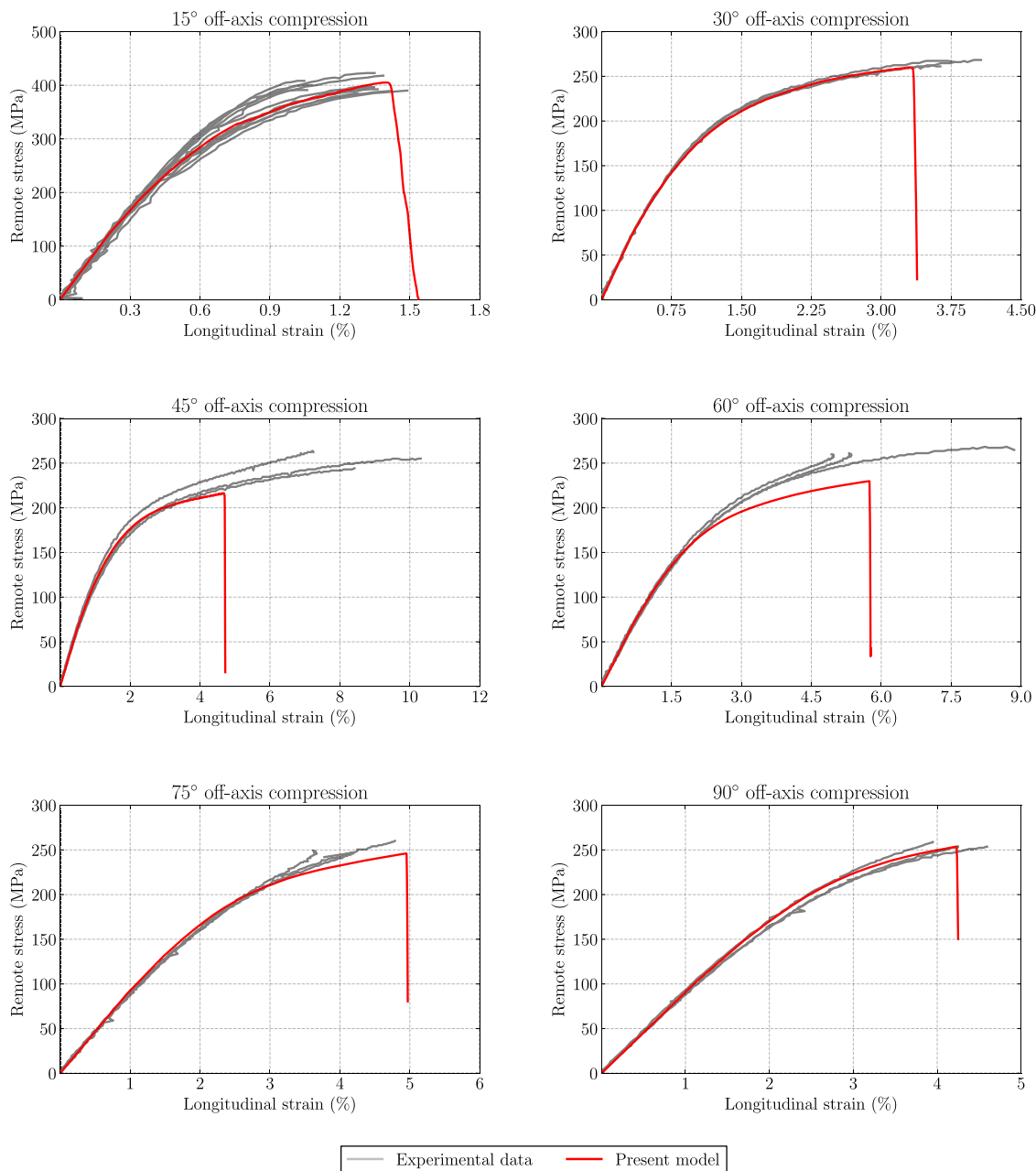
Fig. 5. Numerical–experimental comparison of the remote stress vs. axial strain curves of the off-axis compressive tests performed by Koerber et al. [1].

three material properties are required to define the failure envelope: Y_C, Y_T and S_L, where the latter can be experimentally estimated using different methods. Camanho et al. [35] estimated S_L using the ASTM D 3518/3518M-94 test standard [41]. Therefore, S_L was estimated from an in-plane shear test using a [±45°] laminate when 5% of the axial strain is reached (it is not physically measured). However, Koerber et al. [1] estimated S_L by decomposing the failure strength into the transverse normal stress and shear stress in the material direction from off-axis compressive tests at $\theta = 15°$ and 30°, see [42]. Consequently, there are discrepancies when setting S_L, hence, the value can be adjusted within a range ($S_L = [92.3, 99.9]$ MPa) to improve the failure strength predictions. In this study, S_L is defined from Camanho et al. [35], to be consistent with the definition of the input damage parameters of the polymer coming from the same work. In addition, it should be mentioned that a small discrepancies in the failure strength produces a large disagreement in the ultimate axial strain.

A good accuracy of the predicted plastic deformation with respect to the experimental data is obtained, except at $\theta = 60°$ where the hardening response is slightly underpredicted. This numerical-experimental discrepancy at $\theta = 60°$ is because the yield surface does not properly fit the experimental data at that orientation, similar to the damage envelope at $\theta = 45°$ and 60° in Fig. 6.

The predicted fracture planes are compared with those experimentally obtained in Fig. 7, where the fully damaged elements are represented with a dark transparent colour. The predicted fracture planes are in good agreement with the experimental data reported, except for $\theta = 15°$. For this angle, the damage growth is consistent with the experimental data until the peak load, then the fracture angle suddenly changes. The prediction of the fracture planes for $\theta = 15°$ can be improved by orienting the mesh with the fibre angle.

The comparison between the numerical and experimental data from off-axis tensile tests performed by Koerber et al. [2] is carried out. The in-plane dimensions of the specimens for $\theta = 15°$ are 8 mm × 72 mm
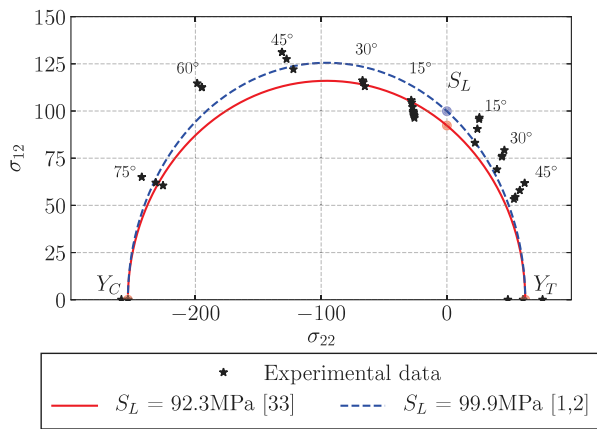
Fig. 6. Failure envelope for the $\sigma_{22} - \sigma_{12}$ stress space with S_L from Camanho et al. [35] and with S_L from Koerber et al. [1], and compressive and tensile experimental data from Koerber et al. [1,2], respectively.

and for $\theta = 30°, 45°$ and $90°$ are 8 mm × 62 mm. The specimen are made with 12 plies. The same boundary conditions as the previous simulations are used applying tension instead of compression, see Fig. 4a. Good correlation between the numerical and experimental data for the plastic deformation is obtained, see Fig. 8. However, the numerical model underpredicted the failure strength for $\theta = 15°, 30°$ and $45°$, since the experimental data are outside the failure envelope, see Fig. 6.

4.2. Open-hole tests

The experimental data from the open-hole compressive and tensile tests carried out by Bessa [43] and by Camanho et al. [35], respectively, are used to further evaluate the accuracy of the proposed constitutive model. The hole diameters used in the tests were: 2 mm, 3 mm, 4 mm and 5 mm in compression, and 2 mm, 4 mm, 6 mm and 8 mm in tension. The in-plane dimensions were defined using a width-to-diameter ratio equals to 6 and the laminate thickness with a stacking sequence of $[90/0/\pm45]_{3S}$. The ends of the virtual specimens are clamped to reproduce the boundary conditions of the tests, see Fig. 4b.

The predicted remote failure strengths are compared with the experimental data in Fig. 9. The numerical results for the tensile tests are within the experimentally measured dispersion, except for the test with a hole diameter equals to 2 mm where a relative error of 2.8% is obtained. The numerical results of the compressive simulations with small hole diameters (2 mm and 3 mm) are within the experimental data scatter, but for higher hole diameters (4 mm and 5 mm) overpredictions are obtained (the highest relative error is 1.9%).

The influence of the plasticity on the numerical results of the open-hole compressive tests with hole diameters equal to 2 mm and 3 mm is analysed, since the rest of the configurations have a large dependence on the longitudinal direction where the plasticity is not considered, see the experimental data reported by Camanho et al. [44]. Similar numerical values of the failure strength are obtained when plasticity is not considered (difference less than 5%). However, the ultimate strain presents large discrepancies (difference within 11% and 13%). The smallest ultimate strains are obtained when plasticity is not considered.
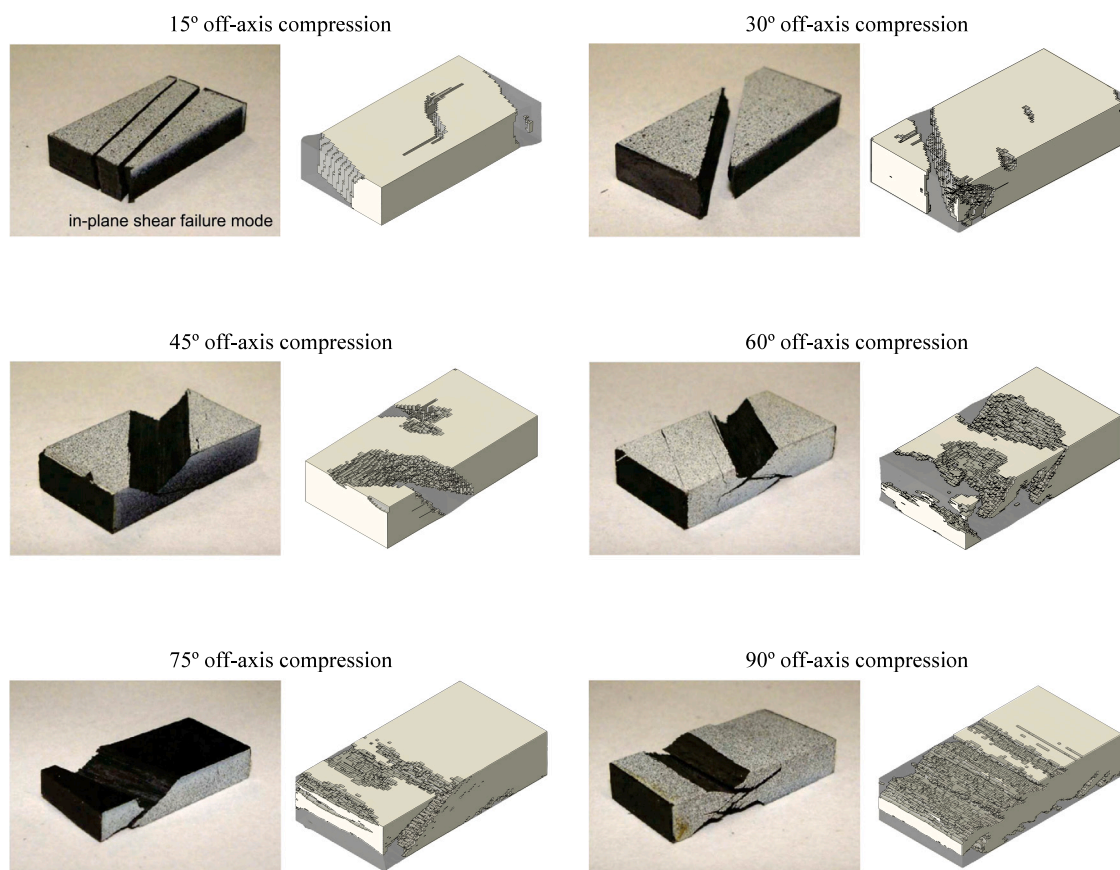
15º off-axis compression

30º off-axis compression

45º off-axis compression

60º off-axis compression

75º off-axis compression

90º off-axis compression

Fig. 7. Numerical-experimental comparison of the fracture planes obtained from the off-axis compressive tests.
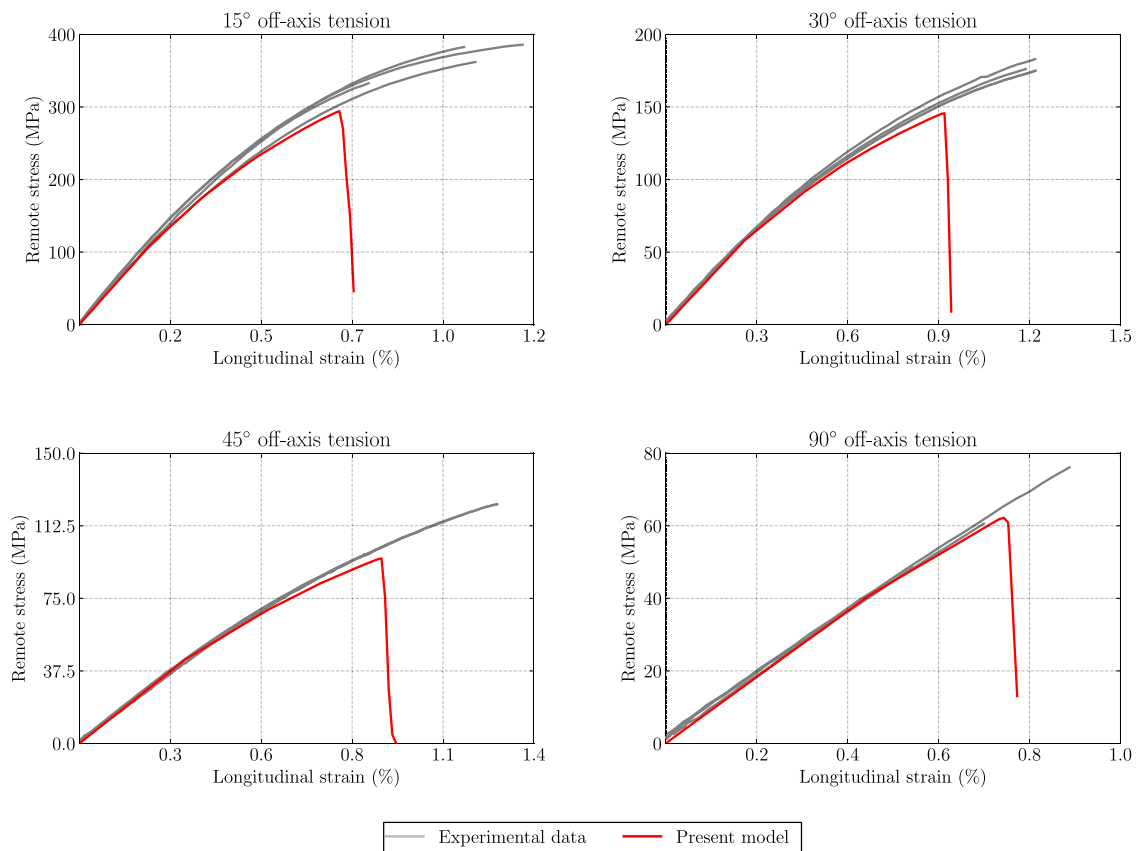
Fig. 8. Numerical-experimental comparison of the remote stress vs. axial strain curves of the off-axis tensile tests performed by Koerber et al. [2].
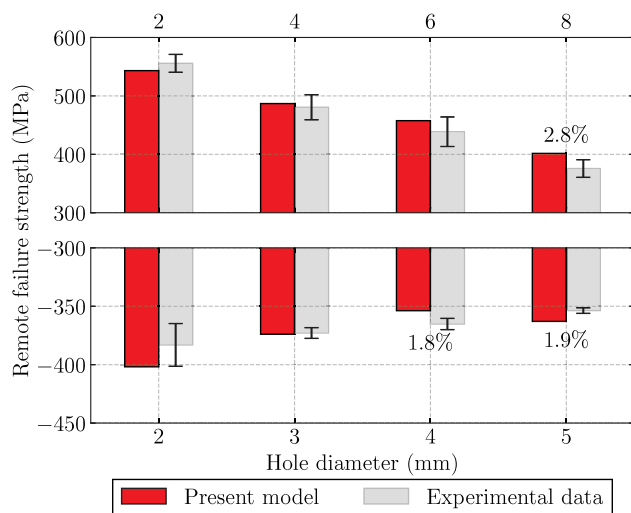

Fig. 9. Numerical-experimental comparison of the failure strength of the open-hole compressive and tensile tests measured by Bessa [43] and by Camanho et al. [35], respectively. The error bars denote the standard deviation of the experimental data and numbers are the relative error between the numerical result and experimental data.

setting the plastic envelope shape coefficients. The new non-associated flow rule used in the plasticity modelling enables the plastic Poisson's ratios and the volumetric plastic strains to be imposed. In addition, the failure criteria can be modified by setting the damage envelope shape coefficients. The main novelty of this work is that using a single constitutive model can be described the plastic deformation and fracture of a large range of materials.

The constitutive model was implemented in a commercial finite element code. Guidelines were provided to calibrate the numerical parameters of the model. The remaining input model parameters can be experimentally obtained from standard tests. The capabilities of the formulation proposed were demonstrated with four tests: off-axis compressive and tensile tests, and open-hole compressive and tensile tests. The comparison between the numerical and experimental data showed a satisfactory agreement of the plastic deformation and the failure strength. In addition, the model properly predicted the fracture plane from off-axis compressive tests.

The material model can be used to simulate the mechanical response of thermoset-based composite materials under quasi-static loading conditions, as well as for thermoplastic-based composites at which the plastic behaviour could be more significant. The present constitutive model can also be applied for the prediction of cases where the out-of-plane stress state governs the mechanical response of the structure, such as filled hole specimens with a preloaded bolt, interlaminar shear strength test, etc. These capabilities will be demonstrated as future work. The model will be extended to account for the viscous effects and capture the strain rate dependencies. This is particularly important for thermoplastic-based composites materials that show a strong dependence on the strain rates. This can be done in a straightforward way based on the generalised Maxwell model for the visco-elastic effects and the Perzyna overstress function for the visco-plastic effects.

5. Conclusions

A new 3D constitutive model to predict the plastic deformation and the progressive failure of unidirectional laminated composite materials was developed and implemented. A new yield function and a new plastic potential function were proposed in conjunction of existing loading functions. The shape of the yield surface can be modified by

CRediT authorship contribution statement

I.R. Cózar: Conceptualization, Methodology, Validation, Formal analysis, Investigation, Writing – original draft, Writing – review & editing. **F. Otero:** Conceptualization, Methodology, Validation, Formal analysis, Investigation, Writing – review & editing, Supervision. **P. Maimí:** Conceptualization, Methodology, Validation, Formal analysis, Investigation, Writing – review & editing, Supervision. **E.V. González:** Conceptualization, Methodology, Validation, Formal analysis, Investigation, Writing – review & editing, Supervision. **S. Miot:** Conceptualization, Methodology, Validation, Formal analysis, Investigation, Writing – review & editing, Supervision. **A. Turon:** Conceptualization, Methodology, Validation, Formal analysis, Investigation, Writing – review & editing, Supervision. **P.P. Camanho:** Conceptualization, Methodology, Validation, Formal analysis, Investigation, Writing – review & editing, Supervision.

Declaration of competing interest

The authors declare the following financial interests/personal relationships which may be considered as potential competing interests: Albert Turon and Emilio Gonzalez reports financial support was provided by European Commission. Pere Maimi and Albert Turon reports financial support was provided by Ministerio de economia y competitividad, Gobierno de España. Ivan Cozar reports financial support was provided by Agència de gestió d'ajuts universitaris i de recerca, govern de Catalunya.

Data availability

The authors are unable or have chosen not to specify which data has been used.

Acknowledgements

Appendix. Algorithm for explicit finite element solver

This appendix presents the algorithm of the present constitutive model used within an explicit finite element solver at Gauss-point level in Algorithm 1.

Algorithm 1: Algorithm of the present constitutive model at time $t_{(n+1)}$

Input:

total deformation at $t_{(n+1)}$: $\boldsymbol{\varepsilon}_{(n+1)}$

internal variables at $t_{(n+1)}$: $\boldsymbol{\varepsilon}^p_{(n)}, \bar{\varepsilon}^p_{(n)}, r_{\ell T_{(n)}}, r_{\ell C_{(n)}}, r_{t_{(n)}}$

Initialisation:

Local Newton–Raphson iteration: $k = 0$

Effective stress tensor: $\tilde{\sigma} = \mathbb{C}_{e0}(\boldsymbol{\varepsilon}_{(n+1)} - \boldsymbol{\varepsilon}^p)$

Effective stress invariants Eqs. (5)–(8)

Loading functions Eqs. (24)–(26)

Elastic domain threshold Eq. (27)

Damage variables Eqs. (28)–(33)

Elastic predictor: $\boldsymbol{\sigma}^{tr}_{(n+1)} = \mathbb{C}_e(\boldsymbol{\varepsilon}_{(n+1)} - \boldsymbol{\varepsilon}^p_{(n)})$

1   **if** $d_t = 0$ *and* $d_{s\ell} = 0$ *and* $d_{st} = 0$ **then**

    Yield stresses: $Y_{CP}(\bar{\varepsilon}^p_{(n)})$, $Y_{TP}(\bar{\varepsilon}^p_{(n)})$ and $S_{LP}(\bar{\varepsilon}^p_{(n)})$

    Yield function Eq. (12): $\phi^p_{(n+1)}$

    General convex cutting-plane algorithm (return-mapping):

2     $\boldsymbol{\sigma}^{(k)}_{(n+1)} = \boldsymbol{\sigma}^{tr}_{(n+1)}$

3     $\phi^{p^{(k+1)}}_{(n+1)} = \phi^p_{(n+1)}$

4   **while** $\phi^{p^{(k+1)}}_{(n+1)} > tol$ **do**

      Derivative of the plastic potential function with respect to the stress tensor: $\partial_{\boldsymbol{\sigma}^{(k)}_{(n+1)}} \varphi^p$

      Increment of the consistency parameter Eq. (47): $\Delta\gamma^{(k)}_{(n+1)}$

      Update the plastic strain tensor:

      $\boldsymbol{\varepsilon}^{p^{(k+1)}}_{(n+1)} = \boldsymbol{\varepsilon}^{p^{(k)}}_{(n+1)} + \Delta\gamma^{(k)}_{(n+1)} \partial_{\boldsymbol{\sigma}^{(k)}_{(n+1)}} \varphi^p$

      Update the stress tensor: $\boldsymbol{\sigma}^{(k+1)}_{(n+1)} = \boldsymbol{\sigma}^{(k)}_{(n+1)} - \Delta\gamma^{(k)}_{(n+1)} \mathbb{C}_e \partial_{\boldsymbol{\sigma}^{(k)}_{(n+1)}} \varphi^p$

      Update the equivalent plastic strain:

      $\bar{\varepsilon}^{p^{(k+1)}}_{(n+1)} = \bar{\varepsilon}^{p^{(k)}}_{(n+1)} + \Delta\gamma^{(k)}_{(n+1)} \sqrt{\frac{1}{2}} \left\| \partial_{\boldsymbol{\sigma}^{(k)}_{(n+1)}} \varphi^p \right\|$

      Update yield stresses: $Y_{CP}(\bar{\varepsilon}^{p^{(k+1)}}_{(n+1)})$, $Y_{TP}(\bar{\varepsilon}^{p^{(k+1)}}_{(n+1)})$ and $S_{LP}(\bar{\varepsilon}^{p^{(k+1)}}_{(n+1)})$

      Yield function Eq. (12): $\phi^{p^{(k+1)}}_{(n+1)}$

5       $k = k + 1$

6   **end**

7   **end**

References

[1] Koerber H, Xavier J, Camanho P. High strain rate characterisation of unidirectional carbon-epoxy IM7-8552 in transverse compression and in-plane shear using digital image correlation. Mech Mater 2010;42(11):1004–19.

[2] Koerber H, Kuhn P, Ploeckl M, Otero F, Gerbaud P-W, Rolfes R, Camanho PP. Experimental characterization and constitutive modeling of the non-linear stress-strain behavior of unidirectional carbon–epoxy under high strain rate loading. Adv Model Simul Eng Sci 2018;5(1):17.

[3] Chen Y, Zhao Y, Ai S, He C, Tao Y, Yang Y, Fang D. A constitutive model for elastoplastic-damage coupling effect of unidirectional fiber-reinforced polymer matrix composites. Composites A 2020;130:105736.

[4] Shin E, Pae K. Effects of hydrostatic pressure on in-plane shear properties of graphite/epoxy composites. J Compos Mater 1992;26(6):828–68.

[5] Lankford J. The compressive failure of polymeric composites under hydrostatic confinement. Composites A 1997;28(5):409–18.

[6] Olsson R. A survey of test methods for multiaxial and out-of-plane strength of composite laminates. Compos Sci Technol 2011;71(6):773–83.

[7] Daghighi S, Weaver PM. Three-dimensional effects influencing failure in bend-free, variable stiffness composite pressure vessels. Compos Struct 2021;262:113346.

[8] Hara E, Yokozeki T, Hatta H, Iwahori Y, Ogasawara T, Ishikawa T. Comparison of out-of-plane tensile strengths of aligned CFRP obtained by 3-point bending and direct loading tests. Composites A 2012;43(11):1828–36.

[9] Chen J, Morozov E, Shankar K. A combined elastoplastic damage model for progressive failure analysis of composite materials and structures. Compos Struct 2012;94(12):3478–89.

[10] Sun C, Chen J. A simple flow rule for characterizing nonlinear behavior of fiber composites. J Compos Mater 1989;23(10):1009–20.

[11] Hoffarth C, Khaled B, Shyamsunder L, Rajan S, Goldberg R, Carney KS, DuBois P, Blankenhorn G. Verification and validation of a three-dimensional orthotropic plasticity constitutive model using a unidirectional composite. Fibers 2017;5(1):12.

[12] Tsai SW, Wu EM. A general theory of strength for anisotropic materials. J Compos Mater 1971;5(1):58–80.

[13] Matzenmiller A, Lubliner J, Taylor R. A constitutive model for anisotropic damage in fiber-composites. Mech Mater 1995;20(2):125–52.

[14] Xie J, Fang G, Chen Z, Liang J. An anisotropic elastoplastic damage constitutive model for 3D needled C/C-SiC composites. Compos Struct 2017;176:164–77.

[15] Holthusen H, Brepols T, Reese S, Simon J-W. An anisotropic constitutive model for fiber-reinforced materials including gradient-extended damage and plasticity at finite strains. Theor Appl Fract Mech 2020;108:102642.

[16] Cho J, Fenner J, Werner B, Daniel I. A constitutive model for fiber-reinforced polymer composites. J Compos Mater 2010;44(26):3133–50.

[17] Daniel IM. Yield and failure criteria for composite materials under static and dynamic loading. Prog Aerosp Sci 2016;81:18–25.

[18] Puck A, Schürmann H. Failure analysis of FRP laminates by means of physically based phenomenological models. Compos Sci Technol 1998;58(7):1045–67.

[19] Puck A, Schürmann H. Failure analysis of FRP laminates by means of physically based phenomenological models. Compos Sci Technol 2002;62(12–13):1633–62.

[20] Quintanas-Corominas A, Maimí P, Casoni E, Turon A, Mayugo JA, Guillamet G, Vázquez M. A 3D transversally isotropic constitutive model for advanced composites implemented in a high performance computing code. Eur J Mech A Solids 2018;71:278–91.

[21] Marsden JE, Hughes TJ. Mathematical foundations of elasticity. Courier Corporation; 1994.

[22] Simo JC, Ju J. Strain-and stress-based continuum damage models—I. Formulation. Int J Solids Struct 1987;23(7):821–40.

[23] Welsh JS, Biskner AC, Nelson EE. Experimental and numerical failure predictions of biaxially-loaded unidirectional carbon composite laminates, Vol. 3548. US Air Force Operationally Responsive Space (ORS) Office; 2009, 87117–85776.

[24] Soden P, Hinton M, Kaddour A. Biaxial test results for strength and deformation of a range of E-glass and carbon fibre reinforced composite laminates: failure exercise benchmark data. In: Failure criteria in fibre-reinforced-polymer composites. Elsevier; 2004, p. 52–96.

[25] Simo JC, Hughes TJ. Computational inelasticity, Vol. 7. Springer Science & Business Media; 2006.

[26] Bažant ZP, Oh BH. Crack band theory for fracture of concrete. Matér Constr 1983;16(3):155–77.

[27] González E, Maimí P, Martín-Santos E, Soto A, Cruz P, de la Escalera FM, de Aja JS. Simulating drop-weight impact and compression after impact tests on composite laminates using conventional shell finite elements. Int J Solids Struct 2018;144:230–47.

[28] Soto A, González E, Maimí P, De La Escalera FM, De Aja JS, Alvarez E. Low velocity impact and compression after impact simulation of thin ply laminates. Composites A 2018;109:413–27.

[29] Fenner JS, Daniel IM. Testing the 2-3 shear strength of unidirectional composite. In: Mechanics of composite, hybrid and multifunctional materials, Vol. 5. Springer; 2019, p. 77–84.

[30] Pinho S, Iannucci L, Robinson P. Physically-based failure models and criteria for laminated fibre-reinforced composites with emphasis on fibre kinking: Part I: Development. Composites A 2006;37(1):63–73.

[31] Davila C, Jaunky N, Goswami S. Failure criteria for FRP laminates in plane stress. In: 44th AIAA/ASME/ASCE/AHS/ASC structures, structural dynamics, and materials conference. 2003, p. 1991.

[32] Camanho P, Arteiro A, Melro A, Catalanotti G, Vogler M. Three-dimensional invariant-based failure criteria for fibre-reinforced composites. Int J Solids Struct 2015;55:92–107.

[33] Melro AR. Analytical and numerical modelling of damage and fracture of advanced composites (Ph.D. thesis), University of Porto; 2011.

[34] Lvov G, Kostromytska O. A data-driven approach to the prediction of plasticity in composites. In: Integrated computer technologies in mechanical engineering. Springer; 2020, p. 3–10.

[35] Camanho PP, Maimí P, Dávila C. Prediction of size effects in notched laminates using continuum damage mechanics. Compos Sci Technol 2007;67(13):2715–27.

[36] ABAQUS Inc. User's manual, 2020. Pawtucket, RI, USA; 2020.

[37] Vogler M, Rolfes R, Camanho P. Modeling the inelastic deformation and fracture of polymer composites-Part I: plasticity model. Mech Mater 2013;59:50–64.

[38] González E, Maimí P, Camanho P, Turon A, Mayugo J. Simulation of drop-weight impact and compression after impact tests on composite laminates. Compos Struct 2012;94(11):3364–78.

[39] Catalanotti G, Camanho P, Marques A. Three-dimensional failure criteria for fiber-reinforced laminates. Compos Struct 2013;95:63–79.

[40] Gutkin R, Pinho S. Practical application of failure models to predict the response of composite structures. In: Proceedings of 18th international conference on composite materials. 2011.

[41] ASTM. Standard test method for in-plane shear response of polymer matrix composite materials by tensile test of a ±45° laminate (ASTM D3518 / D3518M-18). West Conshohocken, PA: ASTM International; 2018, p. 1991, URL: www.astm.org.

[42] Tsai J-L, Sun C. Strain rate effect on in-plane shear strength of unidirectional polymeric composites. Compos Sci Technol 2005;65(13):1941–7.

[43] Bessa M. Meso-mechanical model of the structural integrity of advanced composite laminates (Ph.D. thesis), University of Porto; 2010.

[44] Camanho PP, Dávila CG, Pinho ST, Iannucci L, Robinson P. Prediction of in situ strengths and matrix cracking in composites under transverse tension and in-plane shear. Composites A 2006;37(2):165–76.